PHYSICAL REVIEW RESEARCH **6**, 023260 (2024)

Cone beam neutron interferometry: From modeling to applications

D. Sarenac,[1,2,*] G. Gorbet,[3] C. Kapahi,[2,3] Charles W. Clark,[4] D. G. Cory,[2,5] H. Ekinci,[2] D. V. Garrad,[3]
M. E. Henderson,[2,3] M. G. Huber,[6] D. Hussey,[6] P. A. Kienzle,[6] J. D. Parker,[7] R. Serrat,[2,8] T. Shinohara,[7]
F. Song,[7] and D. A. Pushin[2,3,†]

[1]*Department of Physics, University at Buffalo, State University of New York, Buffalo, New York 14260, USA*
[2]*Institute for Quantum Computing, University of Waterloo, Waterloo, Ontario, Canada N2L3G1*
[3]*Department of Physics, University of Waterloo, Waterloo, Ontario, Canada N2L3G1*
[4]*Joint Quantum Institute, National Institute of Standards and Technology and University of Maryland, College Park, Maryland 20742, USA*
[5]*Department of Chemistry, University of Waterloo, Waterloo, Ontario, Canada N2L3G1*
[6]*National Institute of Standards and Technology, Gaithersburg, Maryland 20899, USA*
[7]*J-PARC Center, Japan Atomic Energy Agency (JAEA), 2-4 Shirakata, Tokai, Ibaraki 319-1195, Japan*
[8]*Centre de Formació Interdisciplinària Superior, Universitat Politècnica de Catalunya, 08028 Barcelona, Spain*

(Received 15 October 2023; accepted 9 April 2024; published 10 June 2024)

Phase-grating moiré interferometers (PGMIs) have emerged as promising candidates for the next generation of neutron interferometry, enabling the use of a polychromatic beam and manifesting interference patterns that can be directly imaged by existing neutron cameras. However, the modeling of the various PGMI configurations is limited to cumbersome numerical calculations and backward propagation models which often do not enable one to explore the setup parameters. Here we generalize the Fresnel scaling theorem to introduce a k-space model for PGMI setups illuminated by a cone beam, thus enabling an intuitive forward propagation model for a wide range of parameters and experimental setups. The interference manifested by a PGMI is shown to be a special case of the Talbot effect, and the optimal fringe visibility is shown to occur at the moiré location of the Talbot distances. We derive analytical expressions for the contrast and the propagating intensity profiles in various conditions and provide the first analysis of the PGMI dark-field imaging signal when considering sample characterization. The model's predictions are compared to experimental measurements and good agreement is found between them. Last, we propose and experimentally verify a method to recover contrast at typically inaccessible PGMI autocorrelation lengths. The presented work provides a toolbox for analyzing and understanding existing PGMI setups and their future applications, for example extensions to two-dimensional PGMIs and characterization of samples with nontrivial structures.

DOI: 10.1103/PhysRevResearch.6.023260

I. INTRODUCTION

Outstanding issues in fundamental physics and ongoing advances in material science have created a need for the development of novel interferometry techniques and characterization tools. Neutrons are a powerful probe of nature and materials, as their nanometer-sized wavelengths and electric neutrality enable unique scattering capabilities that are complementary to x rays and electrons [1–3]. The development and deployment of neutron interferometry setups and diffraction components remains a vibrant research field [4–7].

Traditional Mach-Zehnder designs of neutron interferometers enjoyed a long record of success in performing fundamental tests of. nature and exploring neutron interactions [8]. However, the stringent requirements on alignment, environmental isolation, and narrow wavelength acceptance [9–11] have shifted the focus onto grating-based designs that are capable of working in the full field of the neutron beam and require a relatively low amount of isolation [12–18]. These emerging setups employ the "Talbot effect" which describes the self-imaging that occurs after a wave passes through a periodic structure [19]. For example, passing neutrons with wavelength λ through a grating with period p_G induces a self-image of the grating profile after the neutrons propagate a distance of $2p_G^2/\lambda$. A shortcoming in these neutron setups is the fact that they require the placement of an absorption grating at the imaging plane in order to observe the self-image. The self-image from micron-sized gratings is not detectable via typical neutron cameras with resolution $\gtrsim$100 μm.

The newest form of neutron interferometry setups are the phase-grating moiré interferometers (PGMIs) whose optimal fringe visibility occurs with periods on the millimeter scale, thus enabling direct detection with a neutron camera without the need for an absorption grating [20–24]. The PGMIs are composed of exclusively phase gratings and work in the full field of a cone beam [25]. The standard approach to modeling the PGMIs is through the near-field approximation of the Kirchhoff-Fresnel diffraction [20,25,26]. However, the rather large span in the length scales makes the simulation of relevant

---

[*] dusansar@buffalo.edu

[†] dmitry.pushin@uwaterloo.ca

coherent phenomena with cone beam illumination particularly difficult: The typical values include wavelength distributions that peak in the angstrom range, diffraction features on the micrometer scales, and propagation distances that can span several meters. The work presented here addresses this problem by introducing a forward propagation model that can be used to explore complicated geometries and various setup parameters. The model is derived by extending the Fresnel scaling theorem [27] to the illumination of multiple objects and is similar to the k-space formalism in magnetic resonance [28–30].

The paper is structured as follows: Sec. II provides a brief introduction to self-imaging and the Talbot effect. Section III provides the derivation of the k-space model for simulating the cone beam illumination of multiple objects. Analytical equations are provided allowing calculation of the moiré interference pattern intensity profile and fringe visibility for different setup geometries. In Sec. IV we show good agreement with previously published PGMI data for both two-PGMI and three-PGMI setups. In the following two subsections we provide the first analysis of fringe visibility with the use of source gratings and the first analysis of the dark-field imaging (DFI) signal when performing sample characterization with PGMIs. Last, we predict and experimentally verify that it is possible to recover fringe visibility at typically inaccessible interferometer autocorrelation lengths by varying the location of the phase gratings in the setup.

II. PHASE GRATINGS AND THE TALBOT EFFECT

After a neutron passes though a material of thickness h it accumulates a phase shift with respect to passing through vacuum:

$$\alpha = \frac{2\pi(1-n)h}{\lambda} = Nb_c\lambda h, \tag{1}$$

where n is the material's index of refraction and Nb_c is the scattering length density. It follows that a binary phase grating with a 50% duty cycle, an offset of x_1, period p_G, and height h induces a periodic phase shift over the wave front:

$$f(x) = \frac{\alpha}{2}\mathrm{sgn}\left\{\sin\left[\frac{2\pi}{p_G}(x-x_1)\right]\right\}. \tag{2}$$

We first take the case of a collimated beam that is propagating along the z direction and is well approximated by $k_x = 0$, $k_z = |k_r| = k_0 = 2\pi/\lambda$. On propagating through the phase grating the transverse momentum spectra is given by $P(k_x) = |\Psi(k_x)|^2$, where the transverse momentum wave function is given by:

$$\Psi(k_x) = \Psi_j(k_x) * \mathcal{F}\{e^{-if(x)}\}, \tag{3}$$

where

$$\mathcal{F}\{e^{-if(x)}\} = \delta(k_x)\cos\left(\frac{\alpha}{2}\right) + \sin\left(\frac{\alpha}{2}\right)\sum_m \frac{2e^{-ik_G m x_1}}{\pi m}\delta(k_x - mk_G), \tag{4}$$

$k_G = 2\pi/p_G$ is the grating wave vector, $m = \cdots -3, -1, 1, 3\cdots$ are the nonzero diffraction orders from a binary phase grating with a 50% duty cycle, $\Psi_j(k_x)$ is the incoming momentum wave function, $\delta()$ is the Dirac delta function, $\mathcal{F}\{\}$ is the Fourier transform, and $*$ is the convolution operator. The first term in Eq. (4) is the zeroth diffraction order and the second term is the sum over the higher odd orders. A typical diffraction order spectra obtained from Eq. (4) is depicted on Fig. 1(a) and can be extended to multiple gratings as shown in Figs. 1(b) and 1(c). The amplitude terms dictate that for a phase grating with $\alpha = \pi$, i.e., a π phase grating, the zeroth order is suppressed, while $\alpha = \pi/2$ prepares a state which contains an equal amount of the zeroth order and all of the higher orders combined.

To determine the transverse intensity profile as the beam propagates after the phase grating we must take into account the coupling between the momentum in the transverse and propagation directions. From conservation of momentum we can infer that the phase grating effectively rotates each diffraction order in k space. Therefore, the mth diffraction order gains a transverse wave vector of mk_G and its longitudinal wave vector becomes

$$\beta_m = \sqrt{k_0^2 - (mk_G)^2} \approx k_0\left(1 - \frac{m^2k_G^2}{2k_0^2}\right) = \frac{2\pi}{\lambda}\left(1 - \frac{m^2\lambda^2}{2p_G^2}\right), \tag{5}$$

where the right-hand side is obtained via the paraxial approximation; which is valid for the relevant neutron experiments where typically $\lambda \approx 10^{-9}$ m and $p_G \approx 10^{-6}$ m. The total momentum wave function after a collimated beam passes through a phase grating is then given by:

$$\Psi(k_x, k_z) = \delta(k_x, k_z - k_0)\cos\left(\frac{\alpha}{2}\right) + \sin\left(\frac{\alpha}{2}\right)\sum_m \frac{2e^{-ik_G m x_1}}{\pi m}\delta(k_x - mk_G, k_z - \beta_m) \tag{6}$$

and the intensity for any point after the phase grating can be computed from:

$$I(x, z) = |\mathcal{F}^{-1}\{\Psi(k_x, k_z)\}|^2. \tag{7}$$

Using the equations above, we can determine the intensity profile after the phase grating:

$$I(x, z) = \left|\cos\left(\frac{\alpha}{2}\right) + \sin\left(\frac{\alpha}{2}\right)\sum_m \frac{2}{\pi m}e^{-i\left(\frac{m^2k_G^2}{2k_0}\right)z}e^{imk_G(x-x_1)}\right|^2. \tag{8}$$

Here we can note that the phase shifts proportional to m^2 (m) manifest themselves in the intensity profile as a translation along the propagation (transverse) direction. The latter can be obtained by translating the grating along the transverse direction and thus varying x_1. This is commonly referred to as "phase-stepping."

The Talbot effect, or self-imaging, is a near-field phenomenon that is observed after periodic structures are illuminated by waves [19]. It arises from the interference of the diffraction orders before they propagate into the far field and become spatially separated. For special values of z we can retrieve the original wave function and

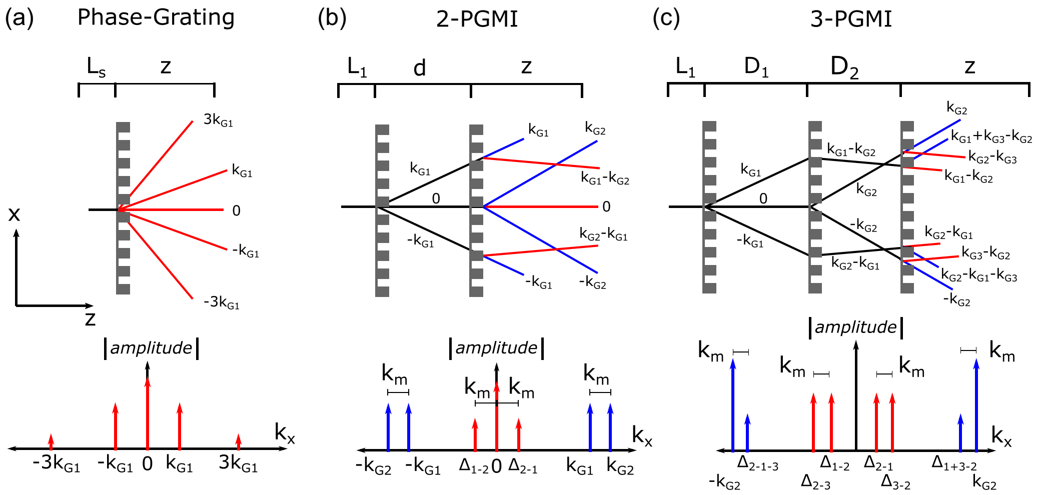

FIG. 1. Central section of the diffraction spectra in phase-grating interferometers for (a) a single binary $\pi/2$ phase grating with 50% duty cycle, (b) two-phase-grating moiré interferometer, and (c) three-phase-grating moiré interferometer. The amplitude of the diffraction orders is dependent on the induced phase shift, in these examples $\alpha = \pi/2$, except for the middle grating of the three PGMI where $\alpha = \pi$. The wave-vector groups that provide the main contribution to a moiré pattern in two-PGMI and three-PGMI are highlighted in red and blue.

thereby achieve self-imaging. Substituting $z = 4\pi k_0/k_G^2 = 2p_G^2/\lambda$ yields $e^{-i2\pi m^2} = 1$ for all integer values of m, and hence the result is equivalent to setting $z = 0$. While setting $z = 2\pi k_0/k_G^2 = p_G^2/\lambda$ yields $e^{-i\pi m^2} = -1$ for all integer values of m, and the only difference is that there is a minus sign in front of the diffraction order sum. This represents the wave function at $z = 0$ where the phase grating has been translated by half a period, as $e^{-imk_Gx_1} = -1$ for all m when $x_1 = p_G/2$. The first and second distances are known as the Talbot ($z_T = 2p_G^2/\lambda$) and half Talbot distance ($z_T/2 = p_G^2/\lambda$), and they are displayed in Fig. 2.

III. *k*-SPACE MODEL FOR CONE BEAMS

The Fresnel scaling theorem states that the intensity obtained with cone-beam illumination of an object can be modeled as a scaled parallel-beam illumination [27]. The theorem dictates a geometrical magnification to the intensity profile as follows: To compute the intensity profile $I(x, z)$ after a propagation of distance z following a previous propagation of distance z_0 we can scale the transverse and longitudinal coordinates as ($x \to x/M, z \to z/M$) where:

$$M = (1 + z/z_0). \tag{9}$$

Here we introduce a k-space model for PGMI setups by extending the Fresnel scaling theorem to the illumination of multiple objects that are spatially separated. In order to do that, we have to consider the geometrical expansion of the wave function $\Psi(k_x, k_z)$ as the cone beam propagates. The model is based on the following set of postulates:

(1) The geometrical scaling of the spatial coordinates in the Fresnel scaling theorem can equivalently be interpreted as an input wave whose wave vector is being scaled with propagation, $k_0 \to k_0/M$. That is, $e^{ik_0(r/M)} = e^{i(k_0/M)r}$. It follows that the transverse and longitudinal wave vectors are being scaled as well: $k_x \to k_x/M$ and $k_z \to k_z/M$; while the angle of propagation remains constant with propagation: $\theta = \sin^{-1}(k_x/k_0) = \sin^{-1}(Mk_x/Mk_0)$.

(2) Each new object with a spatial phase profile of $f(x)$ introduces a convolution between $\mathcal{F}\{e^{-if(x)}\}$ and the incoming momentum-space wave function. That is, each diffraction order of $e^{-if(x)}$ rotates each incoming wave vector to point along a new direction. The previous section outlines this for the case of a single phase grating. We can observe that as a consequence of postulate 1, in a system consisting of two identical phase gratings that are spatially separated, the second phase grating will produce a different amount of rotation compared to the first. Note that in the case of attenuating objects the convolution kernel becomes $\mathcal{F}\{f(x)\}$.

(3) A propagation of distance z induces a phase shift of $e^{ik_zz/M}$ onto each magnified diffraction order.

(4) A new z coordinate (z') is defined after each new object, where $z' = z/M$ is the scaled old coordinate (z) and $z' = 0$ is set at the location of the new object. This extra scaling factor is necessary because the induced phase due to propagation (postulate 3) is not linear with z because the magnification is coupled to the z coordinate. Take for instance the propagation of a distance L_1 followed by propagation of a distance L_2, resulting in a phase of $e^{ik_zL_1/(1+L_1/L_0)}e^{ik_zL_2/[(1+L_1/L_0)(1+L_2/(L_0+L_1)]}$. This is not equivalent to $e^{ik_z(L_1+L_2)/(1+(L_1+L_2)/L_0)}$, which would result from considering a direct propagation distance of $L_1 + L_2$. This behavior is unlike the case of simple plane waves where $e^{ik_zL_1}e^{ik_zL_2} = e^{ik_z(L_1+L_2)}$. The definition of z' rectifies this whereby $e^{ik_zL_1/(1+L_1/L_0)}e^{ik_zL_2/([1+L_2/(L_0+L_1)][1+L_1/L_0]^2)} = e^{ik_z(L_1+L_2)/(1+(L_1+L_2)/L_0)}$.

(5) The intensity profile after the final object is computed according to Eq. (7): $I(x, z) = |\mathcal{F}^{-1}\{\Psi(k_x, k_z)\}|^2$.

(6) The "contrast" or "visibility" of a particular transverse wave vector (k_M) is computed by $V = 2|H(k_M)/H(0)|$, where $H(k_x)$ is the autocorrelation function of $\Psi(k_x)$.

The above postulates allow us to compactly implement a model for a general setup consisting of q objects with

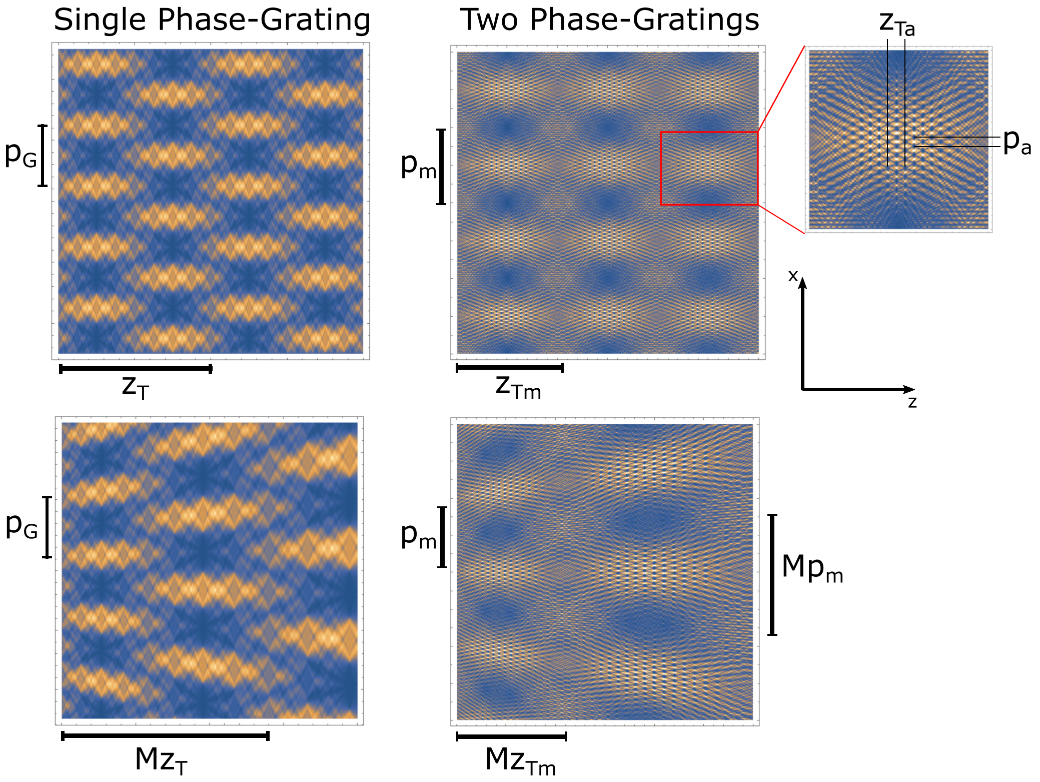

FIG. 2. The top row considers the propagating intensity profile in a parallel beam geometry after a single $\pi/2$ phase grating with period p_G and after two $\pi/2$ phase gratings with slightly different periods manifesting a moiré period of p_m. The single phase grating manifests the well-known Talbot effect whereby a self-image is obtained after a propagation of $z = 2p_G^2/\lambda \equiv z_T$. The interference between the diffraction orders of two phase gratings with slightly different periods gives rise to the moiré period p_m, Talbot-moiré distance z_{Tm}, average period p_a, and average Talbot distance z_{Ta}. The bottom row considers a cone beam geometry whereby the moiré arises even when the two phase gratings have the same period. The moiré parameters are typically observed in a neutron PGMI setup, whereas the higher frequency interference effects (shown in the inset) are not resolved. Last, we can note that in the case of the cone beam illumination the period of the interference patterns as well as the self-imaging distances are continuously magnified by a factor $M = (1 + z/z_0)$, where z_0 is the distance from the source to the last grating.

periodic structures, where the first object is a distance of L_1 from the slit, the second object is a distance of L_2 from the first object, and so on. For an implementation example with the two-PGMI and the corresponding pseudocode, see Appendix 1. The intensity profile after the last object is given by:

$$I(x,z) = \Bigg| \sum_{m_1,m_2\ldots m_q} (a_{m_1} a_{m_2} \cdots a_{m_q}) e^{i\frac{k_0 L_2}{M_1}\cos\theta_{m_1}} e^{i\frac{k_0 L_3}{M_1^2 M_2}\cos\theta_{m_1,m_2}} \cdots e^{i\frac{k_0 L_q}{M_1^2 M_2^2 \ldots M_{q-1}}\cos\theta_{m_1,m_2\ldots m_{q-1}}}$$

$$\times\ e^{i\frac{1}{M_1 M_2 \cdots M_{q-1}}\frac{1}{1+z/(L_1+L_2+L_3+\cdots+L_q)}k_0\left(\frac{z}{M_1 M_2 \ldots M_{q-1}}\cos\theta_{m_1,m_2\ldots m_q} + x\sin\theta_{m_1,m_2\ldots m_q}\right)}\Bigg|^2, \qquad (10)$$

where $z = 0$ is the location of the last object, $\sum_{m_j} a_{m_j}$ are the Fourier coefficients of the jth object, $M_j = 1 + L_{j+1}/(L_1 + L_2 + \cdots + L_j)$ is the scaling factor between object j and $j+1$, and $\theta_{m_1,m_2,\ldots,m_j} = \sin^{-1}[(M_1 M_2 \cdots M_{j-1} k_{G1} + M_1 M_2 \ldots M_{j-2} k_{G2} + \ldots + k_{Gi})/(M_1 M_2 \ldots M_{j-1} k_0)]$ are the diffraction angles after the object j with wave vector k_{Gi}. See Appendix A 2 for a derivation of the two- and three-PGMI intensity profiles.

A. Effects of experiment parameters: Wavelength distribution, slit width, and camera pixel size

The observed interference pattern at the camera is built up by the incoherent sum of each wavelength contribution. Therefore, to account for wavelength spread we can simply integrate over the particular wavelength distribution. Wavelength dependence shows up in the k_0 term as well as the diffraction amplitude terms.

The analysis so far has considered a cone beam from a point source. However, a typical neutron PGMI setup incorporates the use of a slit. Note that the displacement of the point source directly results in a displacement of the interference pattern at the camera. Therefore, the slit manifests an incoherent sum of displaced interference patterns. This can either be accounted for with a straightforward convolution of output intensity with a step function of slit sized width or by integrating the point source location over the slit's width.

The last consideration is the camera resolution. Although the typical values of the effective camera pixel size are relatively large, they are still smaller than the slit size which creates a similar averaging effect. Pixel size can be incorporated through a convolution with a rectangular function or by binning the final intensity into pixel-sized intervals.

B. Fringe visibility or contrast

The "fringe visibility" or "contrast" (V) of the observed intensity profile (I) is a measure of interference, and it is typically defined as:

$$V = \frac{I_{\max} - I_{\min}}{I_{\max} + I_{\min}}. \tag{11}$$

The presented k-space model allows us to determine the intensity profiles at the camera from which we can determine the fringe visibility. Fitting the observed interference pattern to a sinusoid with a specific spatial frequency:

$$I = A + B\cos(2\pi x/p_M + \phi_0), \tag{12}$$

where p_M is the period of the oscillation and ϕ_0 is the phase shift, the fringe visibility of the particular frequency $k_M = 2\pi/p_M$ is given by $V(k_M) = B/A$. In addition to computing the contrast from the fit, the contrast value could also be computed from the Fourier transform of the intensity profile $H(k_x)$, where $V(k_M) = 2|H(k_M)/H(0)|$. Determining the visibility at each pixel using a combination of phase stepping (see Sec. II) and the Fourier transform is a typical procedure.

As per the Wiener-Khinchin theorem, the presented k-space model also allows us to calculate the contrast from the autocorrelation of $\Psi(k_x, k_z)$:

$$\begin{aligned}&\mathcal{F}\{I(x,z) * f_{\text{slit}}(x) * f_{\text{pixel}}(x)\}\\ &\quad = [\Psi(k_x,k_z) * \Psi^*(k_x,k_z)] \times F_{\text{slit}}(k_x) \times F_{\text{pixel}}(k_x).\end{aligned} \tag{13}$$

This result is extremely powerful and makes the determination of contrast computationally straightforward for arbitrary configurations.

IV. OBSERVATIONS AND MODEL APPLICATIONS

A. Moiré of the Talbot effects

The first observation we can make is that the observed interference in a PGMI setup is the moiré of the Talbot effects. Consider the case of a collimated beam illuminating a system of two phase gratings $f_1(x)$ and $f_2(x)$ with different periods p_1 and p_2. It is important to note that the neutron two-PGMI is concerned with phase profiles given by $f_1(x) + f_2(x)$ that results from the sum of two independent binary phase gratings. This is different from the conventional concept of a beat grating with a profile in the form of $\frac{\alpha}{2}\text{sgn}\{\cos[\frac{2\pi}{p_1}(x - x_1)] + \cos[\frac{2\pi}{p_2}(x - x_1)]\}$. The profile of the conventional beat gratings possesses two amplitude values while the profile of $f_1(x) + f_2(x)$ possesses three. With a collimated beam input, the moiré period (p_m), average period p_a, Talbot-moiré distance z_{Tm}, and the average Talbot distance z_{Ta} are given by:

$$p_m = \frac{p_1 p_2}{p_1 - p_2} \quad z_{Tm} = \frac{z_{T1} z_{T2}}{z_{T1} - z_{T2}} = \frac{2p_1^2 p_2^2}{\lambda(p_2^2 - p_1^2)}, \tag{14}$$

$$p_a = \frac{2p_1 p_2}{p_1 + p_2} \quad z_{Ta} = \frac{2z_{T1} z_{T2}}{z_{T1} + z_{T2}} = \frac{4p_1^2 p_2^2}{\lambda(p_1^2 + p_2^2)}. \tag{15}$$

These parameters are depicted on Fig 2.

With cone beam illumination, these parameters get magnified as the cone beam propagates along z: $p_M = Mp_m$, $z_{TM} = Mz_{Tm}$, $p_A = Mp_a$, $z_{TA} = Mz_{Ta}$, where $M = (1 + z/z0)$, see Eq. (9). A typical two-PGMI setup is composed of two gratings with equal periods ($p_1 = p_2 = p_G$), where the distance from the slit to the first grating is L_1, distance between the two gratings is d, and the distance from the second grating to the camera is L_2. We can rewrite the relevant variables at the location of the camera as:

$$p_M = \frac{Lp_G}{d} \quad z_{TM} = \frac{2p_G^2 L(d + L_1)}{\lambda d(d + 2L_1)}, \tag{16}$$

$$p_A = \frac{2Lp_G}{d + 2L_1} \quad z_{TA} = \frac{4p_G^2 L(d + L_1)}{\lambda(d^2 + 2dL_1 + 2L_1^2)}, \tag{17}$$

where $L = L_1 + d + L_2$ is the distance from the slit to the camera. These parameters and their magnification with propagation are depicted on Fig. 2. p_M and z_{TM} are typically observed in a neutron PGMI setup, whereas the higher-frequency interference effects (shown in the inset) are not resolved. It is expected that the development of high-resolution neutron cameras [31] should enable the direct observation of these finer interference effects.

B. Two-PGMI analysis

Let us now consider applying the described k-space model to the previously published works on the two-PGMI. The computational simplicity of the provided equations allows us to compute the contrast of a setup without the need for typical approximations, for example neglecting the $|m| > 1$ terms. We can directly determine the contrast of a two-PGMI setup while taking into account the slit size, wavelength distribution, and camera resolution.

There are three independent two-PGMI setups that were characterized at the National Institute for Standards and Technology Center for Neutron Research (NCNR) [20]. The first setup labeled "Monochromatic" had the following parameters: grating period $p_G = 2.4\,\mu\text{m}$, grating height $h = 9.3\,\mu\text{m}$, $L_1 = 1.2\,\text{m}$, $L = 3.04\,\text{m}$, $\lambda = 4.4$ Å, slit size 200 µm, and camera resolution of 100 µm; the second setup labeled "Bichromatic" had the following parameters: grating period $p_G = 2.4\,\mu\text{m}$, grating height $h = 9.3\,\mu\text{m}$, $L_1 = 1.73\,\text{m}$, $L = 3.51\,\text{m}$, 1/4.2 intensity $\lambda = 2.2$ Å and 3.2/4.2 intensity $\lambda = 4.4$ Å, slit size 200 µm, and camera resolution of 100 µm; the third setup labeled "Polychromatic" had the following parameters: grating period $p_G = 2.4\,\mu\text{m}$, grating height $h = 6.1\,\mu\text{m}$, $L_1 = 4.65\,\text{m}$, $L = 8.36\,\text{m}$, a wavelength distribution

TABLE I. Parameters from the three independent two-PGMI setups that were characterized in Ref. [20]. The "slit fit" is obtained here with the k-space model using a least-squares fit on the slit size. The simulated curves with the best-fitted slit width are shown in Fig. 3.

	L_1 (m)	L (m)	p_G (μm)	h (μm)	Res (μm)	λ (Å)	Slit (μm)	Slit fit (μm)
Mono	1.2	3.04	2.4	9.3	100	4.4	200	230 ± 24
Bi	1.73	3.51	2.4	9.3	100	24% 2.2 and 76% 4.4	200	230 ± 24
Poly	4.65	8.36	2.4	6.1	150	Appendix A 3	500	590 ± 46

somewhat resembling a Maxwell-Boltzmann distribution with $\lambda_c = 5$ Å (see Appendix A 3), slit size 500 μm, and a camera resolution of 150 μm. All of the parameters are listed in Table I.

The comparison between the experimentally measured contrast vs grating separation (d) in these three setups and the simulated contrast using the k-space model is shown in Fig. 3. The simulations are done with a least-squares fit on the slit size to obtain the following best fit values: 230 μm ± 24 μm for Monochromatic and Bichromatic setups and 590 μm ± 46 μm for the Polychromatic setup. Good agreement is found between the measured data and the simulation.

C. Three-PGMI analysis

Given the versatility of the model we can easily explore the three-PGMI setup that was reported in Ref. [22]. Let us consider the setup parameters of Ref. [22]: grating period $p_G = 2.4$ μm, first and third grating height $h = 16$ μm and middle grating height of $h = 30$ μm, distance from the slit to the first grating 4.704 m, distance from first to middle grating 4.6 cm, slit size 500 μm, and a camera pixel size 150 μm. Exploring the contrast for the given parameters with the k-space model shows several interesting features as shown on Fig. 4(a). First, if we consider a monochromatic beam at 5 Å and the first diffraction order approximation, then the contrast profile has the familiar shape and reaches a maximum of 40%. However, if we include the coherence up to the fifth order, then the contrast profile changes and shows a significant dip near the area of the expected maximum contrast. Further modeling can show that the location of the dip varies with the relative position of the middle grating to the middle of the setup $L/2$. This is important to note that if working with a monochromatic, three-PGMI setup as the first-order diffraction approximation is not adequate to describe the behavior. Last, if we account for the polychromatic wavelength distribution shown in Appendix A 3, then the contrast profile is again of the familiar shape even with the higher orders included.

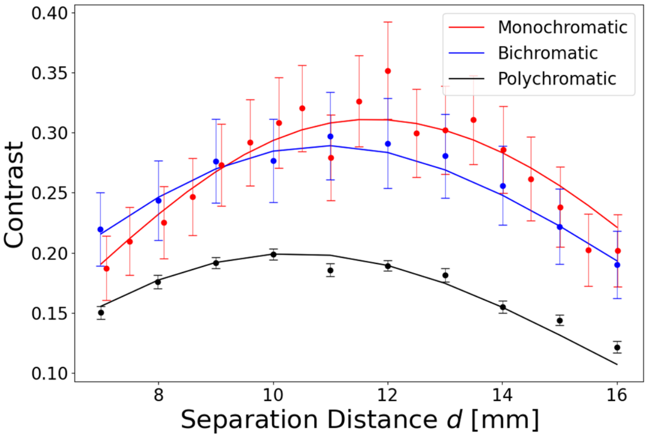

FIG. 3. The experimentally measured contrast data as a function of grating separation (d) reported for the three independent setups in Ref. [20], and the corresponding simulations (lines) done with the k-space model. Data uncertainties shown are purely statistical. The simulations were computed directly with the reported setup parameters and a least-squares fit for the slit size was performed. Good agreement is shown between the simulation and the measurements. All of the PGMI parameters for the three setups are shown in Table I.

The reported contrast in Ref. [22] was 3% and it was surprisingly lower than the expected peak contrast of ≈32%. Reference [32] suggested that the cause of the problem might have been the vertical rotational alignment of the middle grating which possesses a high aspect ratio. The analysis was centered on computing the magnitude of the grating diffraction orders as a function of grating rotation, and extrapolating this change to be a change in maximum obtainable contrast. Here, with the k-space model, we can compute and explore the behavior of the contrast profile directly. Projecting the SEM profile of the middle grating (see Fig. 2 of Ref. [32]) along different angles we can compute the effective profiles that the neutron would see when transversing the rotated grating [33]. Plugging the resulting profile into the model (see Postulate 2 in Sec. III) allows us to simulate the entire system. If we consider the additional degree of freedom of grating rotations, then a good estimate for the observed contrast can be obtained. Shown on Fig. 4(b) is one such example where the first and third grating were rotated around the vertical axis by 3.5° and the middle grating by 4.4°. These misalignments are well within the possible experiment setup errors. The simulation was done with a consideration of diffraction orders spanning from $m = -5$ to 5 in steps of 0.1. This was necessary because the diffraction spectrum of the rotated grating contains appreciable amplitudes at noninteger values of diffraction orders.

D. Sample characterization with dark-field imaging

Grating interferometers can be used to measure the microstructure of samples via a technique called DFI. Similarly to spin-echo small-angle neutron scattering (SESANS), it has been shown that in a grating interferometer with monochromatic illumination the ratio of contrast with the sample (V_s) to the contrast without the sample (V_0) is directly proportional to the real space correlation function of the sample ($C[\xi]$) [34–36]:

$$\mathrm{DFI}(\xi) = \frac{V_s(\xi)}{V_0(\xi)} \propto C(\xi), \tag{18}$$

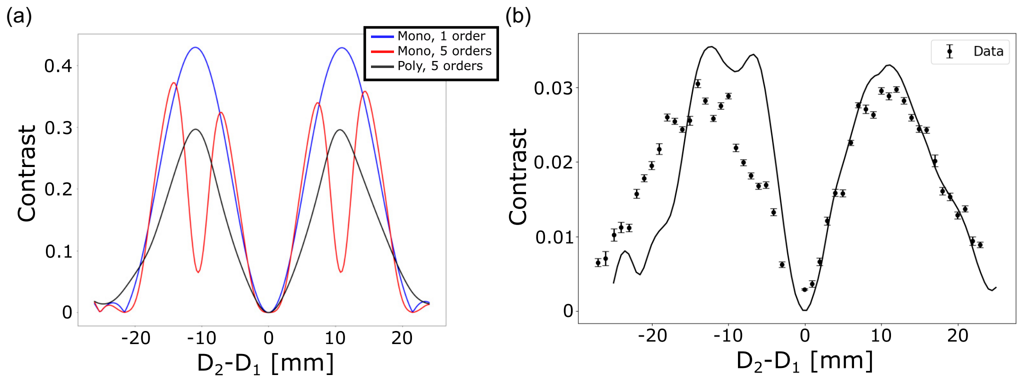

FIG. 4. (a) Simulated contrast for a three-PGMI setup with setup parameters reported as in Ref. [22] but with considering ideal grating shape and alignment. Shown is the case of a monochromatic beam with $\lambda = 5$ Å and with the first and fifth (blue and red) diffraction order approximation. The change in shape with the contrast dip is important to note if working with a monochromatic, three-PGMI setup. The black curve is the simulation that considers the polychromatic wavelength distribution of Ref. [22] (see Appendix A 3) and the fifth diffraction order approximation. Therefore, the measured contrast of ≈3% of Ref. [22] was well below the expected maximum contrast of ≈30%. (b) The middle grating possessed a high aspect ratio and baseball batlike shape (see Fig. 2 of Ref. [32]) thereby increasing the influence of grating rotations about the vertical axis. If we consider the additional degree of freedom of grating rotations, then a good estimate for the observed contrast can be obtained. Shown is one such example where the first and third grating were rotated by 3.5° and the middle grating by 4.4°. These misalignments are well within the possible experiment setup errors.

where

$$\xi = \frac{\lambda L_s}{p_M} = \frac{\lambda L_s d}{p_G L} \tag{19}$$

is referred to as the autocorrelation length of the interferometer and L_s is the distance of the sample to the detector if the sample is downstream of the gratings or the distance to the source if the sample is upstream of the gratings. The DFI measurements therefore involve obtaining the two contrast values as ξ is varied, either by varying the phase-grating separation distance d or the distance between the sample and the detector L_s.

With the k-space model we can easily analyze the effect of a sample on the observed DFI signal for a wide range of parameters. Let us consider the sample to be an ideal 50% duty cycle phase grating with period p_s and phase shift $\phi_s = Nb_c\lambda h$:

$$f_s(x) = \frac{\phi_s}{2}\mathrm{sgn}\left(\sin\left[\frac{2\pi}{p_s}x\right]\right). \tag{20}$$

The top row of Fig. 5 shows the DFI signal (V_s/V_0) as a function of p_s and grating separation d, for sample phase shift of $\phi_s = \pi/2$ and for both the monochromatic and polychromatic cases. Here we can note that the largest contrast drop is obtained for $p_s = p_G$ when the sample is placed near the middle of the setup $L_s \approx L/2$ and the two-PGMI is in the optimal contrast condition of $d = p_G^2/\lambda$. Therefore, the two-PGMI typically probes sample periodicity on the order of the grating period (micrometers) similar to a one grating Talbot-Lau grating interferometer [36] but with the added benefit that the observed contrast is in the moiré regime (millimeters).

The bottom row of Fig. 5 shows the DFI signal for $p_s = p_G$ and various sample phase shifts ϕ_s. The x axis is redefined from d to ξ according to Eq. (19). From the monochromatic case it is evident that the DFI signal (triangular wave) is proportional to the autocorrelation function of the sample profile (square wave) for any p_s. We can derive the equation for the expected DFI signal to be

$$\mathrm{DFI}(\xi) \approx |C[\xi](1 - \cos[\phi_s]) + \cos[\phi_s]|. \tag{21}$$

As seen in the bottom row of Fig. 5, a higher-order harmonic appears for $\phi_s > \pi/2$. This behavior has been observed with the inverse Talbot-Lau setup [37]. The polychromatic case is somewhat different because although each wavelength would produce the autocorrelation function of the sample profile, the amount that each wavelength contributes to the total observed intensity is different and cannot be decoupled without a forward propagation simulation. In order to determine the sample autocorrelation function from polychromatic data one could simply perform the k-space simulation for the exact experimental parameters.

E. Dilute solutions of hard spheres

Due to their presence in numerous applications [38–40], dilute solutions of hard spheres are typically used as a benchmark sample in interferometry measurements [34–36]. Let us consider the case of a sample with thickness t, volume fraction ϕ_V, sphere radius R, and macroscopic scattering cross section $\Sigma = \frac{3}{2}\phi_V(\Delta\rho\lambda)^2 R$, where $\Delta\rho = (Nb_c)_{\mathrm{spheres}} - (Nb_c)_{\mathrm{solution}}$. The real-space correlation function of the sample is given by [41]:

$$C(\xi) = \sqrt{1 - \left(\frac{\xi}{2R}\right)^2}\left[1 + \frac{1}{2}\left(\frac{\xi}{2R}\right)^2\right] + 2\left(\frac{\xi}{2R}\right)^2\left[1 - \frac{1}{4}\left(\frac{\xi}{2R}\right)^2\right]\ln\left[\frac{\left|\frac{\xi}{2R}\right|}{1 + \sqrt{1 - \left(\frac{\xi}{2R}\right)^2}}\right]. \tag{22}$$

Neutrons passing through such a sample can be scattered a various number of times by the hard spheres. The two cases of most interest are "single scattering," where the neutron is

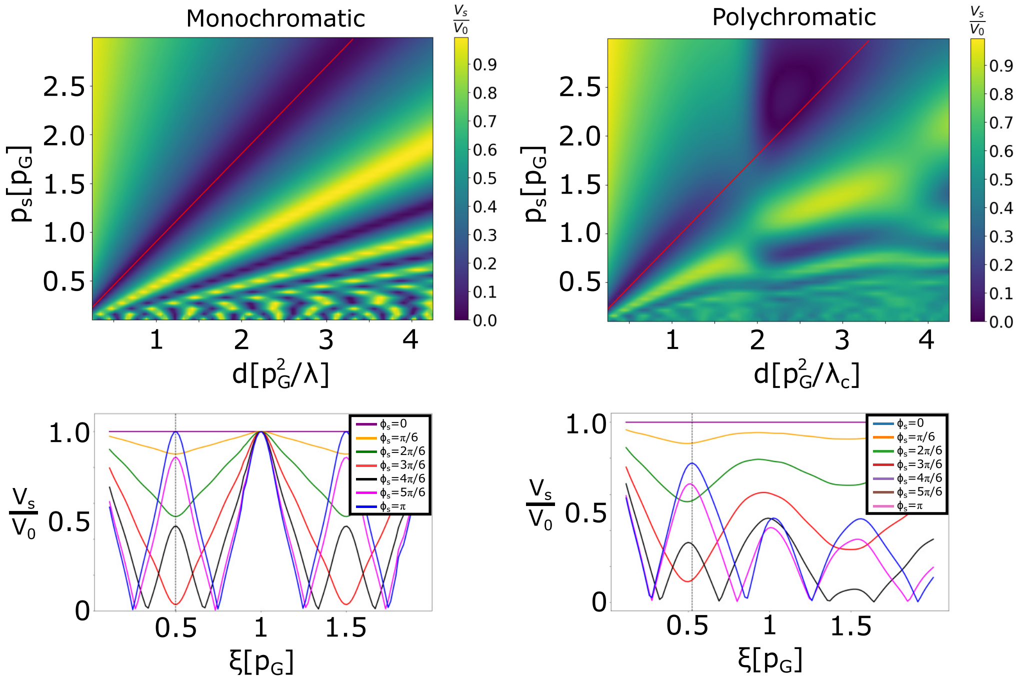

FIG. 5. The simulated two-PGMI DFI signal when considering an ideal phase grating of period p_s and phase ϕ_s as the sample. DFI $= V_s/V_0$ where V_s (V_0) is the contrast with (without) the sample. The left column is for the monochromatic case and the right column is for the polychromatic case (shown in Appendix A 3). The top row shows the DFI dependence on p_s and grating-separation d when $\phi_s = \pi/2$ and $L_s \approx L/2$. The red line along $p_s = 2L_s\lambda d/Lp_G$ shows the location of the highest DFI sensitivity (largest contrast drop). The bottom row shows the dependence of the DFI signal on the interferometer autocorrelation length ξ [see Eq. (19)] for various sample phases ϕ_s when $p_s = p_G$ and $L_s \approx L/2$. The monochromatic case nicely depicts how the DFI signal (triangular wave) is the real space correlation function of the sample (rectangular grating).

scattered zero times or once, and "multiple scattering," where the neutron can be scattered any number of times. From SESANS [42], it has been shown that for a monochromatic beam and single scattering the DFI signal is given by:

$$\mathrm{DFI}(\xi) = 1 + \Sigma t[C(\xi) - 1], \tag{23}$$

and in the multiple scattering limit:

$$\mathrm{DFI}(\xi) = e^{\Sigma t[C(\xi)-1]}. \tag{24}$$

To determine the action of the sample in the k-space model we can note that the transmission probability of a neutron scattered up to M times is given by [43]:

$$T_M = \sum_{j=0}^{M} \frac{1}{j!}(-\Sigma t)^j. \tag{25}$$

Then the neutron transverse wave function after the sample is given by

$$\Psi_{\mathrm{out}}(k_x) = \Psi_{\mathrm{in}}(k_x) * \sqrt{(\delta(k_x)(T_M)^{-M} + \frac{1-T_M^{-M}}{||\mathcal{F}\{C(\xi)\}||}\mathcal{F}\{C(\xi)\})^{*M}}, \tag{26}$$

where $(f)^{*M} = f * f * \cdots * f$ (M times) denotes the convolution power [i.e., $(f)^{*3} = f * f * f$], $||\mathcal{F}\{C(\xi)\}|| = \int|\mathcal{F}\{C(\xi)\}|dk_x$, and $\Psi_{\mathrm{in}}(k_x)$ is the incident wave function. As M corresponds to the maximum number of times an incoming neutron is scattered by the spheres in the sample, we can simply set $M = 1$ to model the single-scattering case and M to be a large value to model the multiple scattering case.

To discretize Eq. (26) for use in a numerical simulation, the $-2R$ to $2R$ range of the correlation function $C(\xi)$ is discretized into $2n + 1$ points. It follows that we have a k-space range of $k_x \in \{-nK, \dots, -K, 0, K, \dots, nK\}$, where $K = \frac{1}{2R}\frac{n}{2n+1}$. The wave function after the sample is then given by:

$$\Psi_{\mathrm{out}}(k_x) = \Psi_{\mathrm{in}}(k_x) * \sqrt{\left(\delta(k_x)(T_M)^{-M} + \sum_{j=-n}^{n}\left[\delta(k_x - jK)\frac{1-T_M^{-M}}{\Omega}\mathcal{F}\{C(\xi)\}\right]\right)^{*M}}, \tag{27}$$

where $\Omega = \sum_{\forall k}|\mathcal{F}\{C(\xi)\}|$. Note that the convolution power used in this expression is now the discrete convolution power.

We are thus enabled to explore the effects of the sample parameters on the DFI signal in a PGMI setup. Figure 6

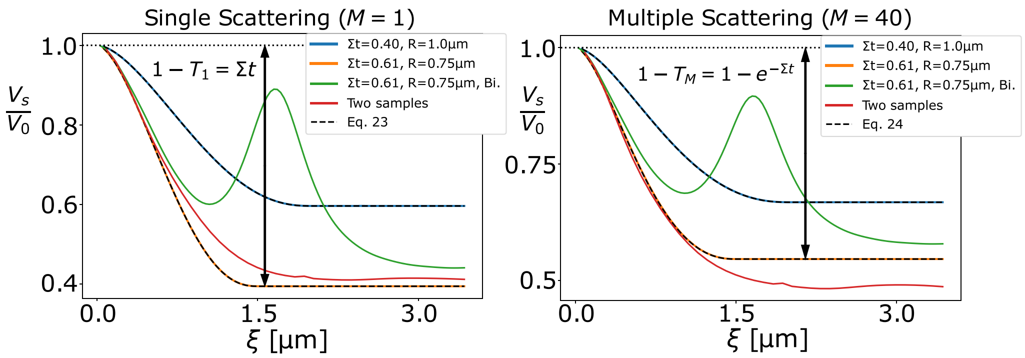

FIG. 6. The DFI signal for the single-scattering case (left) and multiple scattering case (right) using the forward-propagation k-space model. Here we consider a sample of a dilute solution of hard spheres with scattering cross section Σ, sphere radius R, total thickness t, and PGMI parameters $L = 6.0$ m, $L_1 = 3.0$ m, $L_s = 2.0$ m, $p_G = 2.5\,\mu$m, slit width $w_s = 100\,\mu$m, pixel width $w_p = 100\,\mu$m, neutron wavelength of 5 Å, and ideal square gratings of height 15.1 μm (corresponding to a phase shift of $\pi/2$ for neutrons of wavelength 5 Å). Two examples are shown, with $\Sigma t = 0.4,\ 0.61$ and $R = 1.0\,\mu$m, $0.75\,\mu$m, respectively. Furthermore, we show the simulated DFI signal for a bichromatic beam input (green curve) consisting of 50% 2.5 Å and 50% 5 Å. Last, we consider the DFI signal that would be observed when two sequential samples ($\Sigma t = 0.3$, $R = 0.75\,\mu$m, and $\Sigma t = 0.4$, $R = 1.0$ μm) are placed in the beam path of the monochromatic input. The black dashed lines are the expected DFI signals from SESANS Eqs. (23) and (24), showing excellent agreement with the k-space model for the standard experimental configurations. For a monochromatic beam input the the DFI signal beyond $\xi = 2R$ approaches a constant value, with examples marked by the arrow on each plot.

demonstrates how the forward-propagation k-space model reproduces standard results which are in excellent agreement with the known expressions given by Eqs. (23) and (24), and allows for modeling of more complicated geometries including nonmonochromatic wavelength distributions and the consideration of multiple sequential samples with differing parameters.

F. Source grating

One way to increase the number of neutrons that reach the camera is to use an absorption grating as a "source grating," which is essentially an array of slits. Simulating a source grating possessing a period p_c with the k-model can be done through a convolution with the source grating profile in place of the slit as done before, and the outcome is illustrated in Fig. 7. The source grating acts as a notch filter selecting out the contrast for the case where the frequency of the source grating ($2\pi/p_c$) equals a multiple of the observed moiré frequency ($2\pi/p_M$). It can be observed that the contrast is suppressed for $p_M \neq np_c$, while the duty cycle of the source grating determines the amplitude of the max contrast and the presence of the higher-order peaks. Last, we can note that the width (σ) of the contrast peak with the source grating is inversely proportional to the beam size at the source grating.

G. Maximum contrast conditions

The source grating is a powerful addition to a PGMI setup due to the increased neutron flux. It follows that it would be desirable to increase the maximum contrast at each particular grating separation distance. From Fig. 2 it is apparent that maximal contrast of the two-PGMI occurs at $L_2 = z_{TM}/2$, where $L_2 = L - d - L_1$ is the distance from the second grat-

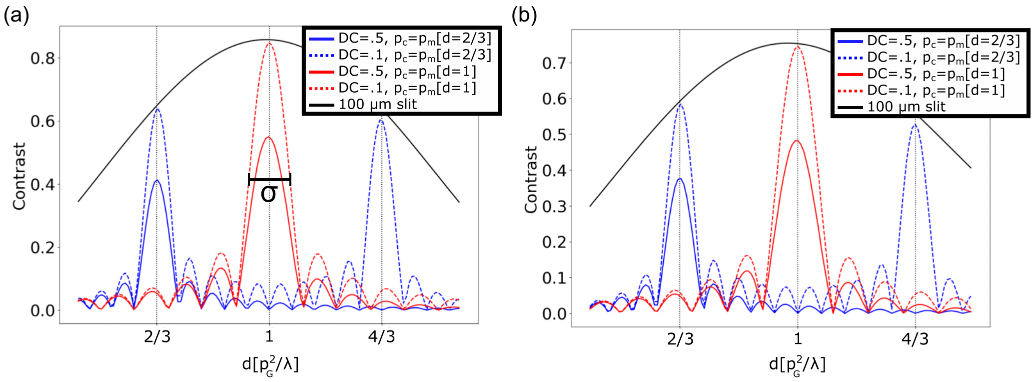

FIG. 7. The source grating acts as a notch filter selecting out contrast for the case where the frequency of the source grating ($2\pi/p_c$) equals a multiple of the observed moiré frequency ($2\pi/p_M$). Plotted are three cases of source grating duty cycle (DC) that demonstrate the effect on filtered contrast and decreased ability to filter higher harmonics with increased duty cycle. (a) The case for a monochromatic beam and (b) for a polychromatic wavelength distribution that is shown in Appendix A 3. The width (σ) of the spectrum with the source grating is inversely proportional to the beam size at the source grating. The shown example is for the consideration of an input beam covering 10 source grating periods.

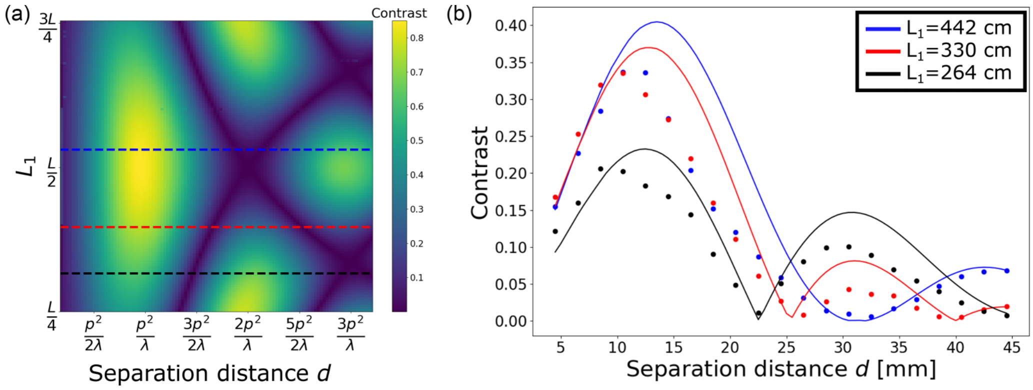

FIG. 8. (a) Ideal contrast vs grating separation distance behavior as the distance from the slit to the first grating (L_1) is varied. (b) To test this prediction an experiment was performed with a pulsed neutron beam and setup parameters: grating period $p_G = 3$ μm, grating height $h = 8.53$ μm, camera resolution of 100 μm, and the wavelength distribution is shown Appendix A 3, where the time of flight was set to select the 5- to 6-Å wavelength range indicated. Note that the phase gratings with $h = 8.53$ μm were fabricated to act as $\pi/2$ phase gratings for 9 Å neutrons. The model fit parameters that were optimized are $L = 8.36$ m, slit size 450 μm, and $L_1 = \{4.42\,\text{m}, 3.30\,\text{m}, 2.64\,\text{m}\}$ for the three cases.

ing to the camera and z_{TM} is given by Eq. (16). Therefore we can calculate the conditions for maximal contrast given the parameters of a particular setup. With a fixed L, the maximal contrast occurs for

$$L - d - L_1 = \frac{p_G^2 L(d + L_1)}{\lambda d(d + 2L_1)}. \tag{28}$$

With the approximation of $L_1 \gg d$ we get:

$$d \approx \frac{L p_G^2}{2\lambda(L - L_1)} \approx \frac{p_G^2}{\lambda} = \frac{z_T}{2}, \tag{29}$$

where for the approximation on the right we used $L_1 = L/2$. In other words, in order for the camera in the two-PGMI setup to be located at the optimal contrast location of $z_{TM}/2$ when the gratings are in the middle of the setup, the second grating needs to be at the half-Talbot distance ($z_T/2$) of the first grating.

From Eq. (16) we can note that the moiré period at the camera is independent of L_1 and L_2 when L is fixed. Therefore, when the camera stays at a constant distance away from the source, as is the case in typical setups, as d is varied the contrast will oscillate according to camera's location relative to $z_{TM}/2$. One approach to maintain higher contrast is to vary L_1 with d:

$$L_1 = L\left(1 - \frac{p_G^2}{2d\lambda}\right) = L\left(1 - \frac{z_T}{4d}\right). \tag{30}$$

Using the k-space model we can explore this idea to determine several interesting conclusions. Figure 8(a) shows the contrast behavior as a function of L_1 and d. To test this prediction an experiment was performed with a pulsed neutron beam at the Energy-Resolved Neutron Imaging System (RADEN) [44], located at beam line BL22 of the Japan Proton Accelerator Research Complex (J-PARC) Materials and Life Science Experimental Facility (MLF). The setup parameters were grating period $p_G = 3$ μm, grating height $h = 8.53$ μm, camera resolution of 100 μm, and the wavelength distribution is shown Appendix A 3, where the time of flight was set to select out the 5- to 6-Å wavelength range indicated. Note that the phase gratings with $h = 8.53$ μm were optimized to act as $\pi/2$ phase gratings for 9 Å neutrons. The model fit parameters that were optimized are $L = 8.36$ m, slit size 450 μm, and $L_1 = \{4.42\,\text{m}, 3.30\,\text{m}, 2.64\,\text{m}\}$ for the three cases. The experimental results along with a simulation are shown on Fig. 8(b).

An interesting note that can be shown with the k-space model is that the dark bands of low contrast on Fig. 8(a) are due to the accumulated phase between the two gratings. Hence, to achieve maximal contrast for every grating separation distance requires the removal of the phase evolution between the two gratings. This can be achieved with two gratings without a gap where the period of one grating is larger than that of the other grating. Whereas variable period gratings are easily achieved in optics *in situ* with widely available spatial light modulators [45], the analogous neutron devices are still in their infancy.

V. CONCLUSION

We have developed a toolbox for analyzing neutron interferometers illuminated by cone beams. The model postulates are developed through the generalization of the Fresnel scaling theorem. This forward propagation model allows for analysis of PGMI intensity and contrast given a wide range of setup parameters, nonideal considerations, phase structures, and attenuation structures.

The model was used to simulate experiments with two-PGMI and three-PGMI setups. Good agreement was found, and the enabled optimization provided informative estimates for the parameters that were used in those experiments. In addition, we provide the first analysis of fringe visibility with the use of source gratings and the first analysis of the DFI signal when performing sample characterization with PGMIs. Furthermore, several interesting conclusions were reached. For example, it was shown that the "far-field" interference of PGMIs is a manifestation of a moiré of the Talbot effects from the two phase gratings. Last, the model predicts an oscillation of the contrast as a function of the distance between the first phase grating and the slit. This was experimentally tested and

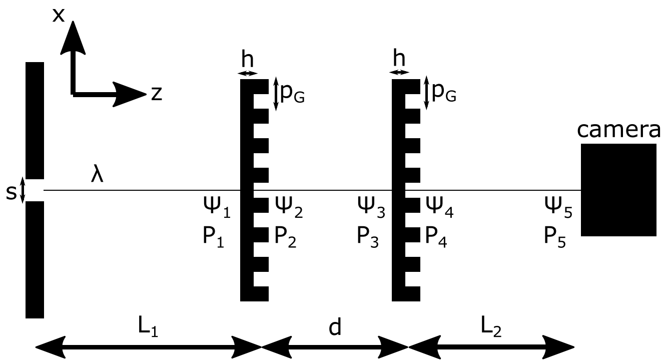

FIG. 9. Two-PGMI setup for the pseudocode example.

confirmed with a two-PGMI at the RADEN facility at the J-PARC.

The introduced model provides a backbone for future extensions, such as two-dimensional phase gratings and characterization of samples with irregular structures. The model naturally enables the exploration of various sample structures and the expected dark-field imaging signal that they would produce. Furthermore, the addition of the orthogonal wave vectors and propagators can be accomplished in analogous fashion to the one-dimensional case presented here [46].

ACKNOWLEDGMENTS

This work was supported by the Canadian Excellence Research Chairs (CERC) program, the Natural Sciences and Engineering Research Council of Canada (NSERC) Discovery program, Collaborative Research and Training Experience (CREATE) program, the Canada First Research Excellence Fund (CFREF), and the National Institute of Standards and Technology (NIST) and the U.S. Department of Energy, Office of Nuclear Physics, under Interagency Agreement No. 89243019SSC000025. The pulsed neutron experiment at J-PARC MLF was performed under a user program (Proposal No. 2022A0104).

APPENDIX

1. Pseudocode example

Here we provide an implementation example of the described k-space model by describing the pseudocode to compute contrast and intensity of a typical two-PGMI. Consider the setup of Fig. 9 with the following parameters: incoming neutrons with wavelength λ, equal period p_G and height h for the two phase gratings, distance from the slit to the first phase grating L_1, distance between the two phase gratings d, distance from the second phase grating to the camera L_2, slit size s, and camera pixel size w.

The initial wave function is taken to be a plane wave with wave vector $k_0 = 2\pi/\lambda$ moving along the z direction: $\Psi_1 = \delta(k_x, k_z - k_0)$. For implementing the model it is convenient to use an array of 2×1 matrices where the first value of each matrix is the transverse wave vector and the second value is the complex amplitude associated with this particular wave vector. Therefore the initial array is

$$P_1 = \{\{0, 1\}\}. \tag{A1}$$

Postulate 2 states that each new object with a spatial phase profile of $f(x)$ introduces a convolution between the incoming wave function and $\mathcal{F}\{e^{if(x)}\}$. After passing through the first phase grating the convolution kernel is given by Eq. (4):

$$\mathcal{F}\{e^{-if(x)}\} = \delta(k_x)\cos\left(\frac{\alpha}{2}\right) + \sin\left(\frac{\alpha}{2}\right)\sum_m \frac{2e^{-ik_G m x_1}}{\pi m}\delta(k_x - mk_G), \tag{A2}$$

where x_1 is the transverse translation of the phase grating which is typically modulated to achieve phase stepping. Let us further simplify the example to consider $\pi/2$ phase gratings, that is, $\alpha = Nb_c\lambda h = \pi/2$. Then after the convolution the array becomes

$$P_2 = \sum_m \{\{mk_G, a_m\}\} = \left\{\cdots\left\{-k_G, -\frac{\sqrt{2}e^{ik_G x_1}}{\pi}\right\}, \left\{0, \frac{1}{\sqrt{2}}\right\}, \left\{k_G, \frac{\sqrt{2}e^{-ik_G x_1}}{\pi}\right\}\cdots\right\}. \tag{A3}$$

Postulate 1 tells us that the propagation from the first grating to the second grating scales the transverse wave vectors as $k_x \rightarrow k_x/M_1$, where $M_1 = 1 + d/L_1$. Postulate 3 tells us that the amplitude of each scaled wave vector picks up a phase of $\text{Exp}[idk_z/M_1] \approx \text{Exp}[idk_0(1 - k_x^2/[2k_0^2])/M_1]$. We can factor out the common phase of $\text{Exp}[idk_0/M_1]$ to get the reduced phase with propagation $\text{Exp}[-idk_x^2/(2k_0M_1)]$. Therefore our updated array becomes

$$P_3 = \left\{\left\{-\frac{k_G}{M_1}, -\frac{\sqrt{2}}{\pi}e^{-idK_z\left[-\frac{k_G}{M_1}, \frac{k_0}{M_1}\right]}\right\}, \left\{0, \frac{1}{\sqrt{2}}\right\}, \left\{\frac{k_G}{M_1}, \frac{\sqrt{2}}{\pi}e^{-idK_z\left[\frac{k_G}{M_1}, \frac{k_0}{M_1}\right]}\right\}\right\}, \tag{A4}$$

where for clarity we have set $x_1 = 0$, displayed only the $m = -1, 0, 1$ diffraction orders, and defined the function for the reduced longitudinal wave vector:

$$K_z[k_x, k_0] = k_x^2/(2k_0). \tag{A5}$$

Similarly to the first phase grating, the second phase grating does the convolution operation between the incoming wave function and Eq. (A2),

$$\begin{aligned} P_4 = \Bigg\{&\left\{-\frac{k_G}{M_1} - k_G, \frac{2}{\pi^2}e^{-idK_z\left[-\frac{k_G}{M_1}, \frac{k_0}{M_1}\right]}\right\}, \left\{-k_G, -\frac{1}{\pi}\right\},\\ &\left\{\frac{k_G}{M_1} - k_G, -\frac{2}{\pi^2}e^{-idK_z\left[\frac{k_G}{M_1}, \frac{k_0}{M_1}\right]}\right\},\\ &\left\{-\frac{k_G}{M_1}, -\frac{1}{\pi}e^{-idK_z\left[-\frac{k_G}{M_1}, \frac{k_0}{M_1}\right]}\right\}, \left\{0, \frac{1}{2}\right\},\\ &\left\{\frac{k_G}{M_1}, \frac{1}{\pi}e^{-idK_z\left[\frac{k_G}{M_1}, \frac{k_0}{M_1}\right]}\right\},\\ &\left\{-\frac{k_G}{M_1} + k_G, -\frac{2}{\pi^2}e^{-idK_z\left[-\frac{k_G}{M_1}, \frac{k_0}{M_1}\right]}\right\}, \left\{k_G, \frac{1}{\pi}\right\},\\ &\left\{\frac{k_G}{M_1} + k_G, \frac{2}{\pi^2}e^{-idK_z\left[\frac{k_G}{M_1}, \frac{k_0}{M_1}\right]}\right\}\Bigg\}. \end{aligned} \tag{A6}$$

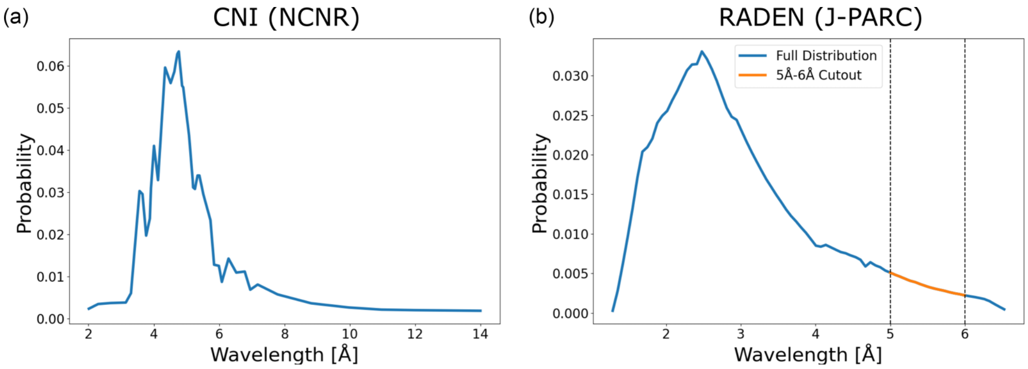

FIG. 10. (a) The wavelength distribution for the Cold Neutron Imaging (CNI) facility at the National Institute of Standards and Technology's Center for Neutron Research (NCNR). This wavelength distribution was used for the simulation shown in Fig. 4(b) and the "polychromatic case" simulations of Figs. 3, 4(a), 5, and 7. (b) The wavelength distribution for the RADEN facility at the J-PARC. The indicated wavelength distribution cutout between 5 and 6 Å was used for the simulations shown in Fig. 8.

Similarly to before, the propagation from the second grating to the camera scales the transverse wave vectors as $k_x \to k_x/M_2$, where $M_2 = 1 + L_2/(L_1 + d)$. Likewise the reduced phase with propagation is $\mathrm{Exp}[-iL_2K_z[\frac{k_x}{M_2}, \frac{k_0}{M_1M_2}]]$, where $k_x = mk_G/M_1$. However, given that $z = 0$ was redefined to start at the second grating we need to add an additional scaling term of M_1 (see postulate 4) and get $\mathrm{Exp}[-iL_2K_z[\frac{k_x}{M_2}, \frac{k_0}{M_1M_2}]/M_1]$. The array then becomes

$$\begin{aligned}P_5 = \Bigg\{&\Bigg\{-\frac{k_G(1+M_1)}{M_1M_2}, \frac{2}{\pi^2}e^{-idK_z\left[-\frac{k_G}{M_1},\frac{k_0}{M_1}\right]}e^{-iL_2K_z\left[-\frac{k_G(1+M_1)}{M_1M_2},\frac{k_0}{M_1M_2}\right]/M_1}\Bigg\}, \Bigg\{\frac{-k_G}{M_2}, -\frac{1}{\pi}e^{-iL_2K_z\left[\frac{-k_G}{M_2},\frac{k_0}{M_1M_2}\right]/M_1}\Bigg\},\\ &\Bigg\{\frac{k_G(1-M_1)}{M_1M_2}, -\frac{2}{\pi^2}e^{-idK_z\left[\frac{k_G}{M_1},\frac{k_0}{M_1}\right]}e^{-iL_2K_z\left[\frac{k_G(1-M_1)}{M_1M_2},\frac{k_0}{M_1M_2}\right]/M_1}\Bigg\}\Bigg\{-\frac{k_G}{M_1M_2}, -\frac{1}{\pi}e^{-idK_z\left[\frac{k_G}{M_1},\frac{k_0}{M_1}\right]}e^{-iL_2K_z\left[-\frac{k_G}{M_1M_2},\frac{k_0}{M_1M_2}\right]/M_1}\Bigg\}, \Bigg\{0, \frac{1}{2}\Bigg\},\\ &\Bigg\{\frac{k_G}{M_1M_2}, \frac{1}{\pi}e^{-idK_z\left[\frac{k_G}{M_1},\frac{k_0}{M_1}\right]}e^{-iL_2K_z\left[\frac{k_G}{M_1M_2},\frac{k_0}{M_1M_2}\right]/M_1}\Bigg\}, \Bigg\{\frac{k_G(M_1-1)}{M_1M_2}, -\frac{2}{\pi^2}e^{-idK_z\left[\frac{k_G}{M_1},\frac{k_0}{M_1}\right]}e^{-iL_2K_z\left[\frac{k_G(M_1-1)}{M_1M_2},\frac{k_0}{M_1M_2}\right]/M_1}\Bigg\},\\ &\Bigg\{\frac{k_G}{M_2}, \frac{1}{\pi}e^{-iL_2K_z\left[\frac{k_G}{M_2},\frac{k_0}{M_1M_2}\right]/M_1}\Bigg\}, \Bigg\{\frac{k_G(M_1+1)}{M_1M_2}, \frac{2}{\pi^2}e^{-idK_z\left[\frac{k_G}{M_1},\frac{k_0}{M_1}\right]}e^{-iL_2K_z\left[\frac{k_G(1+M_1)}{M_1M_2},\frac{k_0}{M_1M_2}\right]/M_1}\Bigg\}\Bigg\}.\end{aligned} \tag{A7}$$

This array contains all of the information about the wave function at the camera: $\Psi_5(k_x) = \sum_n a_n\delta(k_x - k_n)$, where k_n (a_n) is the first (second) entry of each matrix in P_5. As per postulate 5, the intensity is given by $I(x) = |\mathcal{F}^{-1}\{\Psi(k_x)\}|^2$, where $I(x)$ was written out in Eq. (A13).

As per postulate 6, to calculate the contrast of the moiré wave vector k_m, we need to compute $H(k_x) = \Psi_5(k_x) * \Psi_5^*(k_x)$. Following through with our array in the pseudocode we compute $H(k_x) = P_5(k_x) * P_5^*(k_x)$. Note that there will be multiple entries with the same wave vector as different combinations of wave vectors contribute to the interference at a specific frequency. Therefore we need reduce $H(k_x)$ to combine all equal wave-vector entries. For example $H(k_x) = \{\cdots\{k_i, a\}, \{k_i, b\}, \{k_j, c\}, \{k_j, d\}\cdots\} \to H(k_x) = \{\ldots\{k_i, a+b\}, \{k_j, c+d\}\ldots\}$. The contrast for a particular wave vector k_m is given by:

$$V(k_m) = \left|\frac{2H(k_m)}{H(0)}\right|. \tag{A8}$$

Let us say that we wish to integrate the effect of a rectangular slit of width "s" and pixel size "w." Then according to Eq. (13)

$$V(k_m) = \left|\frac{2H(k_m)\mathrm{sinc}(sk_m/2)\mathrm{sinc}(wk_m/2)}{H(0)}\right|. \tag{A9}$$

Last, to incorporate a particular wavelength distribution, for example the one depicted on Fig. 10(a) or Fig. 10(b), one simply needs to calculate $H(k_x) = \int d\lambda p(\lambda)P_5(k_x, \lambda) * P_5^*(k_x, \lambda)$ and follow through to Eq. (A9).

2. Intensity profile equations

After a single object located at L_1 from the slit, the intensity at any point (x, z) after the object can be determined from Eq. (10):

$$I(x, z) = \left|\sum_m a_m e^{i\frac{1}{1+z/L_1}k_0(z\cos\theta_m + x\sin\theta_m)}\right|^2, \tag{A10}$$

which in the paraxial approximation for a 50% duty-cycle phase grating reduces to

$$I(x,z)=\left|\cos\left(\frac{\alpha}{2}\right)+\sin\left(\frac{\alpha}{2}\right)\sum_{m}\frac{2}{\pi m}e^{-imk_Gx_1}e^{-i\left[\frac{m^2k_G^2}{2k_0(1+z/L_1)}\right]z}e^{i\frac{mk_G}{1+z/L_1}x}\right|^2, \tag{A11}$$

where α is given by Eq. (1) and the a_m terms are given in Eq. (4). Note that Eq. (A11) is identical to Eq. (8) with the added feature that the wave vectors are being scaled with propagation $k_x\to k_x/(1+z/L_1)$ and $k_z\to k_z/(1+z/L_1)$. It follows that the size of the self-image as well as the Talbot distance increase with propagation. This is shown in the bottom row of Fig. 2.

Considering the addition of a second object at a distance of L_2 from the first object, the intensity at any location (x,z) after the second object is

$$I(x,z)=\left|\sum_{m,n}a_ma_ne^{i\frac{k_0}{M_1}L_2\cos\theta_m}e^{i\frac{1}{M_1M_2}k_0(\frac{z}{M_1}\cos\theta_{m,n}+x\sin\theta_{m,n})}\right|^2, \tag{A12}$$

where $M_1=1+L_2/L_1$ and $M_2=1+z/(L_1+L_2)$. In the notation of a two-PGMI let us consider a cone beam that travels through the first phase grating located a distance of L_1 away from the slit, followed by free-space propagation of distance d, followed by the second phase grating. In the paraxial approximation we can obtain the intensity profile as the beam propagates further:

$$\begin{aligned}I(x,z)=\Bigg|&\mathcal{C}_1\mathcal{C}_2+\mathcal{C}_1\mathcal{S}_2\sum_{n}\frac{2}{\pi n}e^{ink_G(\frac{x}{M_2}-x_2)}e^{-i\frac{n^2k_G^2}{2k_0M_2}z}+\mathcal{S}_1\mathcal{C}_2\sum_{m}\frac{2}{\pi m}e^{i\frac{m^2k_G^2d}{2k_0M_1}}e^{imk_G\frac{x}{M_1M_2}}e^{-i\frac{m^2k_G^2}{2k_0M_1^2M_2}z}\\&+\mathcal{S}_1\mathcal{S}_2\sum_{n,m}\frac{4}{\pi^2mn}e^{i\frac{m^2k_G^2d}{2k_0M_1}}e^{-ink_Gx_2}e^{i(\frac{mk_G}{M_1}+nk_G)\frac{x}{M_2}}e^{-i\frac{(m/M_1+n)^2k_G^2}{2M_2k_0}z}\Bigg|^2,\end{aligned} \tag{A13}$$

where $\mathcal{S}_j=\sin(\alpha_j/2)$, $\mathcal{C}_j=\cos(\alpha_j/2)$. Equation (A13) gives an analytical expression for the spatial intensity profile after the second grating in a two-PGMI, and it is depicted in the bottom row of Fig. 2. Although one has the freedom to include an arbitrary number of diffraction orders, the seventh orders and above have negligible influence given that the amplitude of the diffraction orders scale with $1/m$.

After three objects the intensity at any location (x,z) after the third object is

$$I(x,z)=\left|\sum_{m,n,\ell}a_ma_na_\ell e^{i\frac{k_0}{M_1}L_2\cos\theta_m}e^{i\frac{k_0L_3}{M_1^2M_2}\cos\theta_{m,n}}e^{i\frac{1}{M_1M_2}\frac{1}{1+z/(L_1+L_2+L_3)}k_0(\frac{z}{M_1M_2}\cos\theta_{m,n,\ell}+x\sin\theta_{m,n,\ell})}\right|^2. \tag{A14}$$

Let us consider a typical three-PGMI setup with slit to first grating, first grating to second grating, and second grating to third grating distances being L_1, L_2, L_3, respectively. In the paraxial approximation for binary phase gratings the intensity after the third grating is given by:

$$\begin{aligned}I(x,z)=\Bigg|&\mathcal{C}_1\mathcal{C}_2\mathcal{C}_3+\mathcal{C}_1\mathcal{C}_2\mathcal{S}_3\sum_{\ell}\frac{2}{\pi\ell}e^{i\ell k_G(\frac{x}{M_3}-x_3)}e^{i\frac{\ell^2k_G^2}{2k_0M_3}z}+\mathcal{C}_1\mathcal{S}_2\mathcal{C}_3\sum_{n}\frac{2}{\pi n}e^{i\frac{n^2k_G^2L_3}{2k_0M_2}}e^{ink_G\frac{x}{M_2M_3}}e^{-i\frac{n^2k_G^2}{2k_0M_2^2M_3}z}\\&+\mathcal{S}_1\mathcal{C}_2\mathcal{C}_3\sum_{m}\frac{2}{\pi m}e^{-i\frac{m^2k_G^2L_2}{2k_0M_1}}e^{i\frac{m^2k_G^2L_3}{2k_0M_1^2M_2}}e^{imk_G\frac{x}{M_1M_2M_3}}e^{-i\frac{m^2k_G^2}{2k_0M_1^2M_2^2M_3}z}\\&+\mathcal{S}_1\mathcal{S}_2\mathcal{C}_3\sum_{n,m}\frac{4}{\pi^2mn}e^{-i\frac{m^2k_G^2L_2}{2k_0M_1}}e^{-i\frac{(m/M_1+n)^2k_G^2L_3}{2k_0M_2}}e^{i(\frac{mk_G}{M_1}+nk_G)\frac{x}{M_2M_3}}e^{-i\frac{(m/M_1+n)^2k_G^2}{2k_0M_2^2M_3}z}+\mathcal{S}_1\mathcal{C}_2\mathcal{S}_3\sum_{m,\ell}\frac{4}{\pi^2m\ell}e^{-i\frac{m^2k_G^2L_2}{2k_0M_1}}e^{-i\frac{m^2k_G^2L_3}{2k_0M_1^2M_2}}e^{-i\ell k_Gx_3}\\&\times e^{i(\frac{mk_G}{M_1M_2}+\ell k_G)\frac{x}{M_3}}e^{-i\frac{(m/M_1+n)^2k_G^2}{2k_0M_2^2M_3}z}+\mathcal{C}_1\mathcal{S}_2\mathcal{S}_3\sum_{n,\ell}\frac{4}{\pi^2n\ell}e^{-i\frac{n^2k_G^2L_3}{2k_0M_2}}e^{-i\ell k_Gx_3}e^{i(\frac{nk_G}{M_2}+\ell k_G)\frac{x}{M_3}}e^{-i\frac{(n/M_2+\ell)^2k_G^2}{2k_0M_3}z}\\&+\mathcal{S}_1\mathcal{S}_2\mathcal{S}_3\sum_{m,n,\ell}\frac{8}{\pi^3mn\ell}e^{-i\frac{m^2k_G^2L_2}{2k_0M_1}}e^{i\frac{m^2k_G^2L_3}{2k_0M_1^2M_2}}e^{i\frac{n^2k_G^2L_3}{2k_0M_2}}e^{-i\frac{(m/M_1+n)^2k_G^2L_3}{2k_0M_2}}e^{-i\ell k_Gx_3}e^{i(\frac{mk_G}{M_1M_2}+\frac{nk_G}{M_2}+\ell k_G)\frac{x}{M_3}}e^{-i\frac{(\frac{mk_G}{M_1M_2}+\frac{nk_G}{M_2}+\ell k_G)^2k_G^2}{2k_0M_3}z}\Bigg|^2.\end{aligned} \tag{A15}$$

This equation is rather general, accommodating arbitrary parameters. Considering a standard three-PGMI setup consisting of $\pi/2, \pi, \pi/2$ phase gratings and a monochromatic input, half of the terms are removed as $\mathcal{C}_2=0$.

3. Wavelength distributions

Here we show the wavelength distributions from the Cold Neutron Imaging (CNI) facility at the National Institute of Standards and Technology's Center for Neutron Research (NCNR), and the wavelength distributions from the RADEN facility at the Japan Proton Accelerator Research Complex (J-PARC).

[1] A. G. Klein and S. A. Werner, Neutron optics, Rep. Prog. Phys. **46**, 259 (1983).

[2] H. Abele, The neutron. its properties and basic interactions, Prog. Part. Nucl. Phys. **60**, 1 (2008).

[3] B. T. M. Willis and C. J. Carlile, *Experimental Neutron Scattering* (Oxford University Press, Oxford, 2017).

[4] C. W. Clark, R. Barankov, M. G. Huber, M. Arif, D. G. Cory, and D. A. Pushin, Controlling neutron orbital angular momentum, Nature (London) **525**, 504 (2015).

[5] D. A. Pushin, M. Arif, and D. G. Cory, Decoherence-free neutron interferometry, Phys. Rev. A **79**, 053635 (2009).

[6] D. Sarenac, M. G. Huber, B. Heacock, M. Arif, C. W. Clark, D. G. Cory, C. B. Shahi, and D. A. Pushin, Holography with a neutron interferometer, Opt. Express **24**, 22528 (2016).

[7] J. Klepp, S. Sponar, and Y. Hasegawa, Fundamental phenomena of quantum mechanics explored with neutron interferometers, Prog. Theor. Exp. Phys. **2014**, 82A01 (2014).

[8] H. Rauch and S. A. Werner, *Neutron Interferometry: Lessons in Experimental Quantum Mechanics, Wave-Particle Duality, and Entanglement* (Oxford University Press, New York, 2015), Vol. 12.

[9] M. Arif, D. E. Brown, G. L. Greene, R. Clothier, and K. Littrell, Multistage position-stabilized vibration isolation system for neutron interferometry, Vibr. Monit. Cont. **2264**, 20 (1994).

[10] P. Saggu, T. Mineeva, M. Arif, D. G. Cory, R. Haun, B. Heacock, M. G. Huber, K. Li, J. Nsofini, D. Sarenac *et al.*, Decoupling of a neutron interferometer from temperature gradients, Rev. Sci. Instrum. **87**, 123507 (2016).

[11] D. A. Pushin, M. G. Huber, M. Arif, C. B. Shahi, J. Nsofini, C. J. Wood, D. Sarenac, and D. G. Cory, Neutron interferometry at the national institute of standards and technology, Adv. High Energy Phys. **2015**, 1 (2015).

[12] J. F. Clauser and S. Li, Talbot-vonLau atom interferometry with cold slow potassium, Phys. Rev. A **49**, R2213(R) (1994).

[13] F. Pfeiffer, C. Grünzweig, O. Bunk, G. Frei, E. Lehmann, and C. David, Neutron phase imaging and tomography, Phys. Rev. Lett. **96**, 215505 (2006).

[14] A. D. Cronin and B. McMorran, Electron interferometry with nanogratings, Phys. Rev. A **74**, 061602(R) (2006).

[15] C. David, B. Nöhammer, H. H. Solak, and E. Ziegler, Differential x-ray phase contrast imaging using a shearing interferometer, Appl. Phys. Lett. **81**, 3287 (2002).

[16] A. D. Cronin, J. Schmiedmayer, and D. E. Pritchard, Optics and interferometry with atoms and molecules, Rev. Mod. Phys. **81**, 1051 (2009).

[17] M. S. Chapman, C. R. Ekstrom, T. D. Hammond, J. Schmiedmayer, B. E. Tannian, S. Wehinger, and D. E. Pritchard, Near-field imaging of atom diffraction gratings: The atomic talbot effect, Phys. Rev. A **51**, R14(R) (1995).

[18] E. Lau, Beugungserscheinungen an doppelrastern, Ann. Phys. **437**, 417 (1948).

[19] H. F. Talbot, LXXVI. facts relating to optical science. No. IV, Philos. Mag. Ser. 3 **9**, 401 (1836).

[20] D. A. Pushin, D. Sarenac, D. S. Hussey, H. Miao, M. Arif, D. G. Cory, M. G. Huber, D. L. Jacobson, J. M. LaManna, J. D. Parker *et al.*, Far-field interference of a neutron white beam and the applications to noninvasive phase-contrast imaging, Phys. Rev. A **95**, 043637 (2017).

[21] D. S. Hussey, H. Miao, G. Yuan, D. Pushin, D. Sarenac, M. G. Huber, D. L. Jacobson, J. M. LaManna, and H. Wen, Demonstration of a white beam far-field neutron interferometer for spatially resolved small angle neutronscattering, arXiv:1606.03054.

[22] D. Sarenac, D. A. Pushin, M. G. Huber, D. S. Hussey, H. Miao, M. Arif, D. G. Cory, A. D. Cronin, B. Heacock, D. L. Jacobson *et al.*, Three phase-grating moiré neutron interferometer for large interferometer area applications, Phys. Rev. Lett. **120**, 113201 (2018).

[23] A. J. Brooks, D. S. Hussey, H. Yao, A. Haghshenas, J. Yuan, J. M. LaManna, D. L. Jacobson, C. G. Lowery, N. Kardjilov, S. Guo *et al.*, Neutron interferometry detection of early crack formation caused by bending fatigue in additively manufactured ss316 dogbones, Mater. Des. **140**, 420 (2018).

[24] A. J. Brooks, G. L. Knapp, J. Yuan, C. G. Lowery, M. Pan, B. E. Cadigan, S. Guo, D. S. Hussey, and L. G. Butler, Neutron imaging of laser melted SS316 test objects with spatially resolved small angle neutron scattering, J. Imag. **3**, 58 (2017).

[25] H. Miao, A. Panna, A. A. Gomella, E. E. Bennett, S. Znati, L. Chen, and H. Wen, A universal moiré effect and application in x-ray phase-contrast imaging, Nat. Phys. **12**, 830 (2016).

[26] I. Hidrovo, J. Dey, H. Meyer, D. S. Hussey, N. N. Klimov, L. G. Butler, K. Ham, and W. Newhauser, Neutron interferometry using a single modulated phase grating, Rev. Sci. Instrum. **94**, 045110 (2023).

[27] D. Paganin *et al.*, *Coherent X-ray Optics* (Oxford University Press on Demand, Oxford, 2006).

[28] A. Sodickson and D. G. Cory, A generalized k-space formalism for treating the spatial aspects of a variety of NMR experiments, Prog. Nucl. Magn. Reson. Spectrosc. **33**, 77 (1998).

[29] D. G. Cory, J. B. Miller, A. N. Garroway, and W. S. Veeman, Chemical-shift-resolved back-projection imaging, J. Magn. Reson. (1969) **85**, 219 (1989).

[30] N. F. Ramsey, A molecular beam resonance method with separated oscillating fields, Phys. Rev. **78**, 695 (1950).

[31] D. S. Hussey, J. M. LaManna, E. Baltic, and D. L. Jacobson, Neutron imaging detector with 2 µm spatial resolution based on event reconstruction of neutron capture in gadolinium oxysulfide scintillators, Nucl. Instrum. Methods A **866**, 9 (2017).

[32] B. Heacock, D. Sarenac, D. G. Cory, M. G. Huber, D. S. Hussey, C. Kapahi, H. Miao, H. Wen, and D. A. Pushin, Angular alignment and fidelity of neutron phase-gratings for improved interferometer fringe visibility, AIP Adv. **9**, 085115 (2019).

[33] B. Heacock, D. Sarenac, D. G. Cory, M. G. Huber, J. P. W. MacLean, H. Miao, H. Wen, and D. A. Pushin, Neutron

sub-micrometre tomography from scattering data, IUCrJ **7**, 893 (2020).

[34] R. Andersson, L. F. Van Heijkamp, I. M. De Schepper, and W. G. Bouwman, Analysis of spin-echo small-angle neutron scattering measurements, J. Appl. Crystallogr. **41**, 868 (2008).

[35] S. K. Lynch, V. Pai, J. Auxier, A. F. Stein, E. E. Bennett, C. K. Kemble, X. Xiao, W.-K. Lee, N. Y. Morgan, and H. H. Wen, Interpretation of dark-field contrast and particle-size selectivity in grating interferometers, Appl. Opt. **50**, 4310 (2011).

[36] M. Strobl, General solution for quantitative dark-field contrast imaging with grating interferometers, Sci. Rep. **4**, 7243 (2014).

[37] Y. Kim, D. Kim, D. S. Hussey, J. Kim, M. Mirzaei, D. A. Pushin, C. W. Clark, and S. W. Lee, Analysis of a silicon comb structure using an inverse talbot–lau neutron grating interferometer, Sci. Rep. **12**, 3461 (2022).

[38] J. Qiu, P. H. C. Camargo, U. Jeong, and Y. Xia, Synthesis, transformation, and utilization of monodispersed colloidal spheres, Acc. Chem. Res. **52**, 3475 (2019).

[39] C. P. Royall, P. Charbonneau, M. Dijkstra, J. Russo, F. Smallenburg, T. Speck, and C. Valeriani, Colloidal hard spheres: Triumphs, challenges and mysteries, arXiv:2305.02452.

[40] Y. Xia, B. Gates, Y. Yin, and Y. Lu, Monodispersed colloidal spheres: Old materials with new applications, Adv. Mater. **12**, 693 (2000).

[41] T. Krouglov, I. M. De Schepper, W. G. Bouwman, and M. T. Rekveldt, Real-space interpretation of spin-echo small-angle neutron scattering, J. Appl. Crystallogr. **36**, 117 (2003).

[42] M. T. Rekveldt, W. G. Bouwman, W. H. Kraan, O. Uca, S. V. Grigoriev, K. Habicht, and T. Keller, Elastic neutron scattering measurements using Larmor precession of polarized neutrons, in *Neutron Spin Echo Spectroscopy: Basics, Trends and Applications* (Springer, Berlin, 2003), pp. 87–99.

[43] J. t. Schelten and W. Schmatz, Multiple-scattering treatment for small-angle scattering problems, J. Appl. Crystallogr. **13**, 385 (1980).

[44] T. Shinohara, T. Kai, K. Oikawa, T. Nakatani, M. Segawa, K. Hiroi, Y. Su, M. Ooi, M. Harada, H. Iikura *et al.*, The energy-resolved neutron imaging system, raden, Rev. Sci. Instrum. **91**, 043302 (2020).

[45] J. E. Curtis, B. A. Koss, and D. G. Grier, Dynamic holographic optical tweezers, Opt. Commun. **207**, 169 (2002).

[46] D. Sarenac, G. Gorbet, C. W. Clark, D. G. Cory, H. Ekinci, M. E. Henderson, M. G. Huber, D. Hussey, C. Kapahi, P. A. Kienzle *et al.*, Phase and contrast moiré signatures in two-dimensional cone beam interferometry, arXiv:2311.02261.